Check for updates

RESEARCH ARTICLE

NANO · MICRO small
www.small-journal.com

Multi-Amino Triarylamines for Electrochromic and Electrofluorochromic Applications with Exceptional Stability and Extraordinary Fluorescence Modulation

*Yu-Jen Shao, Peng-Yi Lin, Chin-Hsuan Lin, Cha-Wen Chang, Yu-Ting Kao, William Sun, Yu-Jie Wang, and Guey-Sheng Liou**

This study investigates arylamine small molecules functionalized with multiple primary amino groups and various extended π bridges (TPPA-2N, TPPA-4N, and TPB-4N) to evaluate their opto-electrochemical behaviors. TPPA-4N exhibits polyelectrochromic features and outstanding stability during continuous cyclic voltammetry scans, maintaining 99.0% reversibility after 15 000 cycles and 95.2% reversibility after 10 000 cycles at the first and second oxidation states, respectively. After being fabricated into devices, the TPPA-4N/HV device retains 96% stability after 1000 switching cycles at the first oxidation state and 500 cycles at the second oxidation state, respectively. In addition, the TPPA-4N/HV device also exhibits a blue emission at the neutral state with an exceptional intensity contrast ratio (ICR) of up to 950-fold for electrofluorochromic (EFC) applications, resulting from well-controlled absorption-emission modulation that causes the self-absorption effect. Additionally, the TPB-4N/HV device reveals a moderate ICR of 393-fold. By blending TPPA-4N and TPB-4N, the resulting EFC device exhibits a highly reversible two-stage EFC behavior, transitioning from lime to olive green emission and then completely quenching with gratifying ICR values at each emitting color.

1. Introduction

Electrochromism (EC) is a fascinating phenomenon that has garnered significant attention in academic and industrial research communities.[1–5] It refers to reversible optical changes (color or transparency) of redox-active materials under a suitable applied voltage. These characteristics have gained numerous potential applications in cutting-edge technological advancements, particularly in smart windows, low-energy displays, and adaptive camouflage systems. While EC in early research focused on inorganic materials such as transition metal oxides (e.g., tungsten oxide[6–9] or titanium oxide[10–12]), organic EC materials have gained prominence in recent decades.[13–15] Organic materials are lightweight, flexible, and can be processed through low-cost fabricating methods such as solution casting and printing, realizing roll-to-roll production.[2,3,16–18] Additionally, organic EC materials can be engineered at the molecular level to achieve specific optical and electronic properties. Therefore, researchers could tailor properties such as color range, switching speed, and stability.[19–22] This level of control is challenging to realize with inorganic materials, making organics an attractive and imperative option for advanced applications.

Beyond EC monitoring via absorption mode, electrofluorochromism (EFC) can be utilized to provide an additional light-stimuli mode display under UV irradiation, manifesting reversible modulation of fluorescence intensity upon electrochemical stimulation.[23–25] The ideal EFC materials aspire to acquire high photoluminescence (PL) intensity or quantum efficiency (PLQY) to facilitate achieving an extraordinary emission intensity contrast ratio (ICR), rapid response time, and long shelf life during the redox switching process. Generally, EFC mechanisms and materials can be classified into two categories for design and preparation: i) dyads (or triads) consisting of a redox unit and a fluorophore separated by a spacer[26–28] and ii) intrinsically electroactive fluorophores.[29–34] Triarylamine (TAA) architectures have captured significant attention due to their intrinsically electroactive properties, functional versatility, and flexibility. They allow for fine-tuning of absorption color changes for EC and emission color modulation for EFC applications, and could seamlessly integrate these two functions to enable dual-application potential.[19,31,35] Organic small molecule-based EFC devices (EFCDs) typically perform lower emission ICR than those derived from polymers because of a concentration gradient of the

Y.-J. Shao, P.-Y. Lin, C.-H. Lin, Y.-T. Kao, W. Sun, Y.-J. Wang, G.-S. Liou
Institute of Polymer Science and Engineering
National Taiwan University
No. 1, Sec. 4, Roosevelt Rd., Taipei 10617, Taiwan
E-mail: gsliou@ntu.edu.tw

C.-W. Chang
Department of Digital Printing Materials
Division of Applied Chemistry, Material and Chemical Research Laboratories
Industrial Technology Research Institute
321 Kuang Fu Rd., 2nd Sec., Hsinchu 300044, Taiwan

The ORCID identification number(s) for the author(s) of this article can be found under https://doi.org/10.1002/smll.202508301

DOI: 10.1002/smll.202508301

 © 2025 Wiley-VCH GmbH

electroactive species from the electrode to the bulk solution upon the oxidation/reduction process, which means the difficulty in completely oxidizing/reducing. The remaining emission intensity from the non-oxidized/reduced species could be detected, resulting in low ICR values of the devices (**Figure 1a**).[32,36,37] Conversely, polymer-based EFCDs are dense films in which all chromophores can be fully oxidized/reduced, realizing the complete emission quenching and achieving high ICR values.

Aromatic primary amine (Ar–NH_2) was generally considered an unfavorably active functional group under the electrochemical process; thus, the primary amino group often undergoes further reaction or modification to avoid side reactions, such as imine,[38–41] amide,[42–44] or imide.[45–47] Nevertheless, our group recently reported that *para*-amino-substituted triphenylamine (TPA) derivatives could reveal exceptional stability during the electrochemical and EC process via intervalence charge transfer (IV-CT) to stabilize the primary amine with lone pairs and result in lowering the oxidation potential gratifyingly.[48] Despite synthesizing multiple *para*-amino-substituted triphenylamines (TPAs) with two to four electroactive sites, the resulting materials primarily demonstrated variations in color intensity rather than a broader spectrum of distinct color changes. This limited diversity in color modulation within the same material highlights a significant challenge in the development of EC. We are committed to addressing this weakness and providing a solution by extending the TPA to various TAA architectures. Drawing from our knowledge and experience, we anticipate that expanding the arylamine framework will enhance the degree of EC color modulation and enable the realization of multi-color change capabilities, thereby broadening the potential applications of these materials. Based on these results, the motif of this study is to design and develop three derivatives of multiple *para*-amino-substituted TAA derivatives (**TPPA-2N**, **TPPA-4N**, and **TPB-4N**), as shown in Figure 1b. Multiple primary amino groups could be expected to enrich color modulation and enable lower oxidation potentials. These TAA derivatives exhibited promising PL emission intensities in high-polarity solutions with moderate PLQY, indicating their suitability for EFC applications.

Additionally, we proposed a strategy to enhance the ICR value in small-molecule EFC systems: the oxidized TAA could absorb its own residual emission via a self-absorption effect (Figure 1c). For example, **TPPA-4N** could generate a new absorption band during the oxidation procedure at the exact wavelength range as the emission wavelength of the neutral **TPPA-4N** that facilitates quenching the emission intensity caused by self-absorption effect, leading to minimizing the negative impact from non-oxidized residual molecules in the device and achieving the highest ICR value of the corresponding EFCD (**TPPA-4N/HV**) with 950 folds. Furthermore, when merging **TPPA-4N** and **TPB-4N**, the resulting **TPPA/TPB/HV** EFCD exhibited two-stage emission color changes, enabling the intriguingly pivotal fluorochromism by applying tunable electrical potentials.

2. Results and Discussions

2.1. Electrochemical Behaviors of TTA Derivatives

Three *para*-amino-substituted TTA derivatives were used and synthesized in this study: *N,N″*-bis(4-aminophenyl)-*N,N″*-di(4-methoxyphenyl)-1,4-phenylenediamine (**TPPA-2N**),[49] *N,N,N″, N″*-tetra(4-aminophenyl)-1,4-phenylenediamine (**TPPA-4N**),[50] and *N,N,N″,N″*-tetra(4-aminophenyl)-4,4′-biphenyldiamine (**TPB-4N**)[51] according to the previous references. The codes of **TPPA** and **TPB** represent phenyl and biphenyl π-bridges between two central nitrogen atoms, and 2N and 4N indicate the number of *para*-aminophenyl arms within the molecular structures. Differential pulse voltammetry (DPV) showed that **TPPA-2N** reveals four distinct oxidation peaks at 0.32, 0.58, 1.04, and 1.72 V, consisting of the four electroactive nitrogen sites (two arylamine centers and two primary amino groups), as depicted in **Figure 2a**. Likewise, **TPPA-4N** exhibits six distinct peaks at 0.19, 0.44, 0.76, 0.89, 1.02, and 1.70 V, and its first oxidation (0.19 V) is lower than that of **TPPA-2N**, implying that the amino group features a stronger electron-donating capability than the methoxy group. However, only three peaks at 0.45, 0.75, and 1.64 V appeared for **TPB-4N**, which is different from the expected six peaks and **TPPA-4N**. We inferred that more than one electron transfer should be represented by the single oxidation peak in the DPV diagram, which will be explained and supported by the Nernst equation later. Additionally, when comparing the first oxidation potential, **TPPA-4N** (0.19 V), which features a phenyl π-bridge, also displayed a lower value than TPB-4N (0.45 V), which features a biphenyl π-bridge. This phenomenon could be attributed to the stronger donating ability of the two electroactive nitrogen atoms with a shorter π-bridge, resulting in a lower applied potential. Cyclic voltammetry (CV) was utilized to investigate the first two oxidation potentials and elucidate the reversibility and stability of the amino-functionalized TAAs. As illustrated in Figure 2b, **TPPA-2N** revealed two anodic peaks at 0.31 and 0.56 V and two corresponding cathodic peaks at 0.23 and 0.49 V with the potential difference (ΔE) of 0.08 and 0.07 V, respectively. As amino groups replaced two methoxy substituents, **TPPA-4N** exhibited lower oxidation potentials in both the first and second oxidation states, located at 0.17 and 0.42 V for oxidation and 0.10 and 0.35 V for reduction, with a 0.07 ΔE value equally for these two redox couples. The anodic peaks of **TPB-4N** revealed higher oxidation potentials at 0.44 and 0.77 V, along with larger ΔE values of 0.14 and 0.17 V for the first and second redox couples, respectively (Figure 2c). According to the CV results summarized in **Table 1**, the effect of the number of electroactive amino groups and π bridges on the oxidation potential was elucidated and confirmed.

To clarify the kinetic behaviors of these TAAs, the electrochemical diffusion coefficient (D, $cm^2\ s^{-1}$) was calculated based on the equations shown in the *Supporting Information*. The anodic and cathodic diffusion coefficients for the first two oxidation stages of the **TPPA** series were studied; however, only the first oxidation stage for **TPB-4N** was investigated, due to the indistinguishable peak values at higher scan rates. Based on the Randles-Sevcik equation, all TAA derivatives showed good linear fitting relationships between the square root of the scan rate and the redox peak current (Figures S1–S3, Supporting Information). The calculated diffusion coefficients of **TPPA-2N** and **TPPA-4N** are summarized in Table 1 and exhibit similar high diffusion coefficients. In the first redox process, **TPPA-2N** exhibited $D_a = 2.01 \times 10^{-7}$ and $D_c = 1.45 \times 10^{-7}\ cm^2\ s^{-1}$, and **TPPA-4N** revealed $D_a = 1.97 \times 10^{-7}$ and $D_c = 1.48 \times 10^{-7}\ cm^2\ s^{-1}$. In the second redox process, **TPPA-2N** showed $D_a = 1.21 \times 10^{-7}$ and $D_c = 0.70 \times 10^{-7}\ cm^2\ s^{-1}$, and

© 2025 Wiley-VCH GmbH

16136829, 0, Downloaded from https://onlinelibrary.wiley.com/doi/10.1002/smll.202508301 by National Taiwan University, Wiley Online Library on [12/11/2025]. See the Terms and Conditions (https://onlinelibrary.wiley.com/terms-and-conditions) on Wiley Online Library for rules of use; OA articles are governed by the applicable Creative Commons License

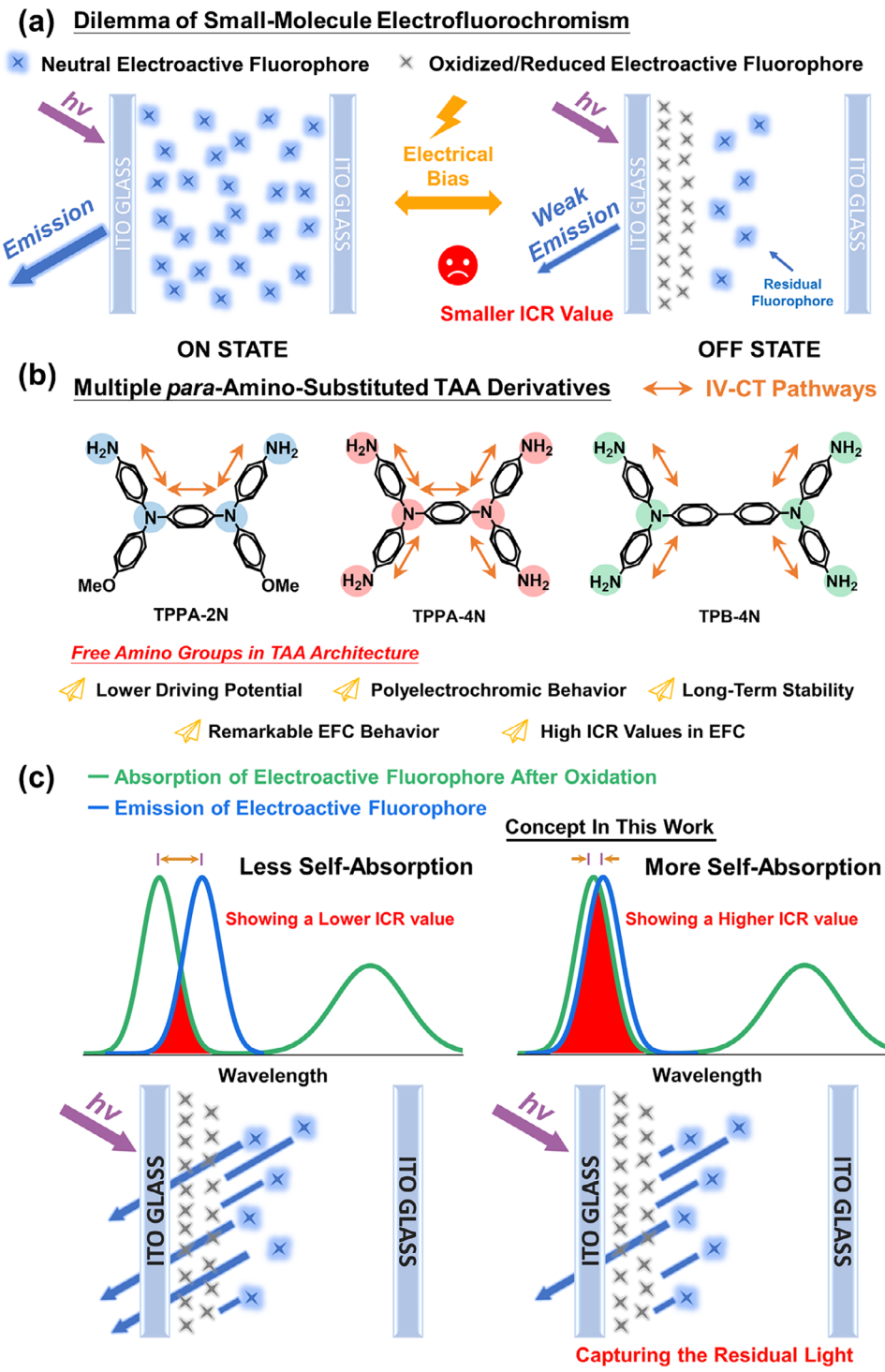

Figure 1. a) Structures of three multiple *para*-amino-substituted TAA derivatives (**TPPA-2N**, **TPPA-4N**, and **TPB-4N**) in this study. b) Schematic presentation of the dilemma of small-molecule electrofluorochromism. c) Schematic presentation of the concept to increase the ICR value in the EFC application.

© 2025 Wiley-VCH GmbH

16136829, 0, Downloaded from https://onlinelibrary.wiley.com/doi/10.1002/smll.202508301 by National Taiwan University, Wiley Online Library on [12/11/2025]. See the Terms and Conditions (https://onlinelibrary.wiley.com/terms-and-conditions) on Wiley Online Library for rules of use; OA articles are governed by the applicable Creative Commons License

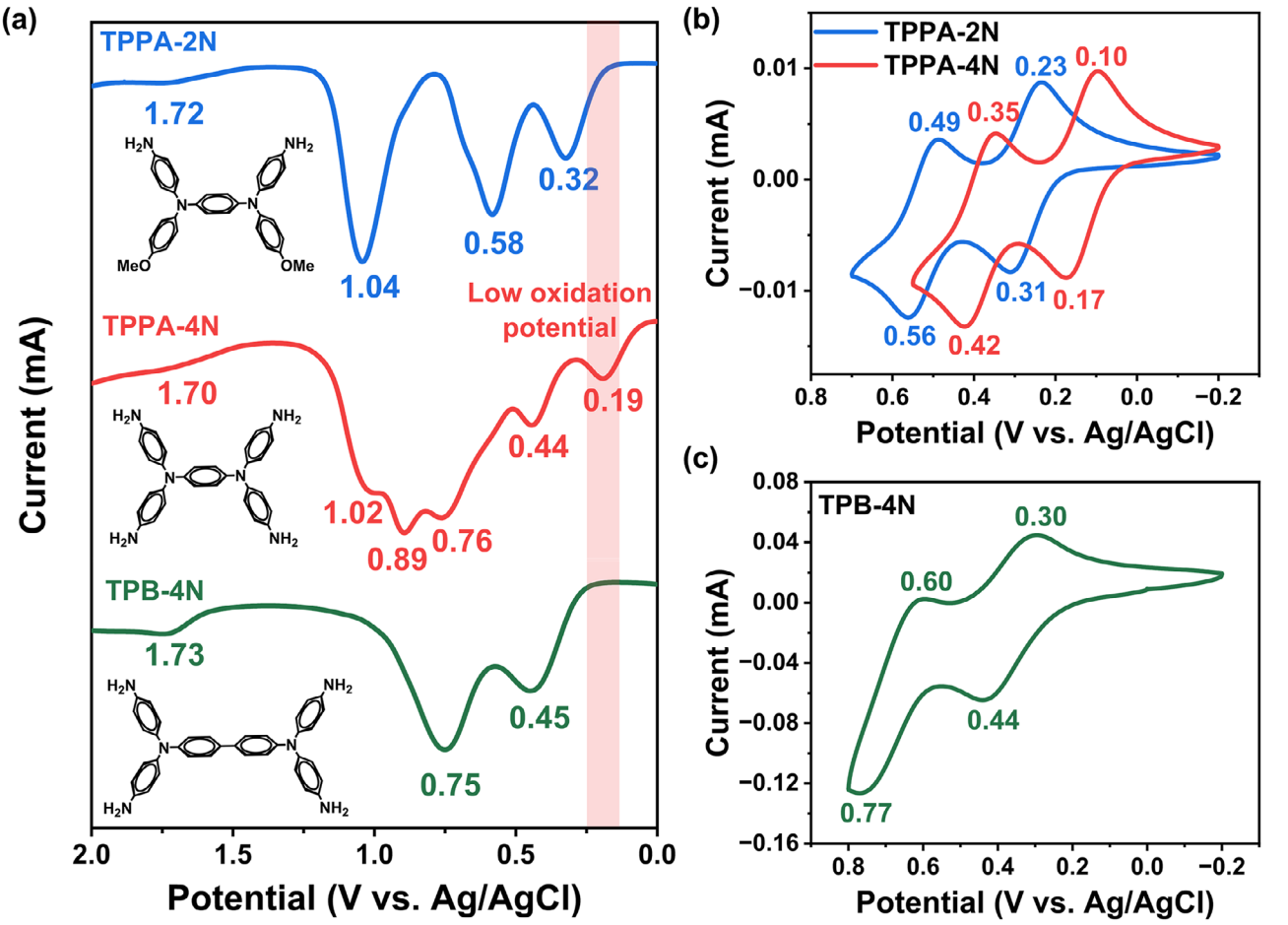

Figure 2. a) DPV diagram of **TPPA-2N, TPPA-4N, TPB-4N** at a scan rate of 4 mV s^{-1}. b,c CV diagrams for b) **TPPA-2N, TPPA-4N**, and c) **TPB-4N** at a scan rate of 50 mV s^{-1}. The measurements were carried out in a quartz cuvette with a 0.6 cm × 2.5 cm ITO-coated glass electrode. (sample amount: 1.75 µmol (5 × 10^{-4} M) in 3.5 mL of 0.1 M $TBABF_4$/GBL).

TPPA-4N exhibited $D_a = 1.27 \times 10^{-7}$ and $D_c = 0.47 \times 10^{-7}$ cm^2 s^{-1}. In comparison, **TPB-4N** displayed lower D values in the first oxidation and reduction processes, indicating that the shorter π-bridge chemical structure could facilitate faster diffusion, which is expected to reflect the EC response capabilities.

2.2. Spectroelectrochemical Analysis

The spectroelectrochemical behaviors were evaluated using an optically transparent thin-layer electrochemical (OTTLE) cell with a sample of 0.5 µmol (5 × 10^{-4} M) in 1 mL of 0.1 M TBAP/GBL. **Figure** 3a–c shows that all TAA derivatives at their neutral state exhibit a transparent and colorless appearance. **TPPA-4N** exhibited a characteristic absorption peak at 317 nm in its neutral state. As the applied voltage increased to 0.4 V, three new peaks appeared at 435, 766, and 983 nm, accompanied by a decrease at 317 nm, and the color changed to a misty green appearance, as depicted in Figure 3b. The weak and broad absorption in the near-infrared (NIR) region ≈983 nm could be ascribed to IV-CT characteristic peaks resulting from the electron coupling between the neutral nitrogen and the cationic radical nitrogen centers. As the applied potential was raised to the second (0.60 V) and third (0.90 V) oxidation states, the absorption peak at 435 nm remained at the same absorbance value. In contrast, the 766 and 983 nm peaks gradually shifted bathochromically and hypsochromically to 802 and 927 nm, respectively, with increasing absorbance values owing to more resonance possibilities to induce IV-CT. As a result, the color changed from mist green to pale green and then to celadon green, accompanied by broadband NIR absorptions. Subsequently, raising the potential to the fourth (1.40 V) and fifth (1.80 V) oxidation stages, the higher doping level structure forms to quench the IV-CT behavior. Therefore, the absorption at 927 nm gradually diminished or even vanished. In addition, the distinct peak at 435 nm in the visible region decreased slightly, while the peak at 802 nm hypsochromically shifted to 744 nm with an enhanced absorbance intensity. Although the fourth and fifth oxidation stages showed a cadet blue appearance, the NIR absorption displayed a significant difference. Thus, **TPPA-4N** could demonstrate a five-stage EC behavior to achieve polyelectrochromic features; in comparison, multiple amino-substituted TPAs in our previous report only displayed one to three-stage coloring behavior (typically light to dense color).[48] **TPPA-2N** also exhibited multi-coloring

© 2025 Wiley-VCH GmbH

16136829, 0, Downloaded from https://onlinelibrary.wiley.com/doi/10.1002/smll.202508301 by National Taiwan University, Wiley Online Library on [12/11/2025]. See the Terms and Conditions (https://onlinelibrary.wiley.com/terms-and-conditions) on Wiley Online Library for rules of use; OA articles are governed by the applicable Creative Commons License

Table 1. The electrochemical properties of TAA derivatives.

Index	1st oxidation state					2nd oxidation state				
	E_{pa} [V] [a]	E_{pc} [V] [b]	ΔE [V] [c]	D_a [d] [× 10^{-7} cm^2 s^{-1}]	D_c [d] [× 10^{-7} cm^2 s^{-1}]	E_{pa} [V] [a]	E_{pc} [V] [b]	ΔE [V] [c]	D_a [d] [× 10^{-7} cm^2 s^{-1}]	D_c [d] [× 10^{-7} cm^2 s^{-1}]
TPPA-2N	0.32	0.23	0.09	2.01	1.45	0.57	0.49	0.08	1.21	0.70
TPPA-4N	0.18	0.09	0.09	1.97	1.48	0.44	0.34	0.10	1.27	0.47
TPB-4N	0.43	0.30	0.13	0.56	0.38	0.77	0.60	0.17	– [e]	– [e]

[a] anodic peak potential (oxidation); [b] cathodic peak potential (reduction); [c] potential difference between anodic and cathodic peaks, | E_{pa} − E_{pc} |; [d] the diffusion coefficient was calculated from the Randles–Sevcik equation; [e] Not available.

behaviors, ranging from colorless to pale green, emerald green, gray-blue, and navy blue (Figure 3a).

Although the methoxy group of **TPPA-2N** has a lower electron-donating ability, the wavelength upon oxidation exhibits more spectral changes in the visible region, specifically ≈600 to 700 nm; the IV-CT characteristic peaks appear in a similar region to those of **TPPA-4N**. Moreover, **TPB-4N** can also exhibit polyelectrochromic features, displaying a three-stage coloring behavior from colorless to pale yellow, green, and then sky blue, as depicted in Figure 3c. Generally, biphenyl π-bridge TPB derivatives exhibit a weaker electron-coupling ability between two electroactive nitrogen centers in the mixed-valence cation radical form, resulting in a longer characteristic absorption wavelength of benzidine-type IV-CT, typically ≈1200 to 1500 nm. In contrast, TPPA derivatives display *p*-phenylenediamine (PPD)-type IV-CT characteristics, with an absorption wavelength of ≈900 to 1100 nm.[19,52–54] However, in this work, the IV-CT characteristic peak of **TPB-4N** appeared at 917 nm instead of the typical longer wavelength above 1200 nm. Hence, we considered that the first oxidation sites are located at the two electroactive nitrogen centers, and the electron coupling might not be dominated through the biphenyl π-bridge to generate benzidine-type IV-CT characteristic absorption. Instead, the cation radical nitrogen would undergo electron coupling with the *para*-aminophenyl arms, thus revealing PPD-type IV-CT characteristic absorption. A similar phenomenon was also reported in the previous report.[55]

As mentioned earlier, **TPB-4N** was speculated to undergo multi-electron transfers in each oxidation state. Thus, we applied a detailed spectroelectrochemical analysis to justify the electron transfer number in each oxidation peak using the Nernst equation Equation (1).

$$E_{appl.} = E_0 + \frac{0.0592}{n} \log\left(\frac{[O]}{[N]}\right) \quad (1)$$

where $E_{appl.}$ is the applied potential, E_0 is the standard potential, n is the number of electrons transferred, and *[O]* and *[N]* are the concentrations of the oxidized/neutral species, respectively. It is not easy to measure or justify the concentrations of the oxidized/neutral species directly; thus, according to Beer's Law (a = εbc), the concentration of the neutralized/oxidized species in the diluted solution should be proportional to the absorbance. Consequently, the absorbance was used to calculate the ratio of oxidized to neutral species, and the detailed calculation method is described in the *Supporting Information*. Figures S4 and S5 (Supporting Information) illustrate the spectroelectrochemical measurements with a stepwise increase in the applied potential for **TPB-4N**, and the electron-transfer results are presented and tabulated in Table S1 (Supporting Information). In the first oxidation state, ranging from 0.42 to 0.58 V, the *n* values were 0.81 and 1.06, indicating that approximately two electrons were transferred simultaneously. Subsequently, with n values of 0.77 + 0.72 + 0.50, approximately two transferred electrons could be estimated to be 0.68 to 1.06 V in the second stage. As a result, combining the results from the spectroelectrochemistry and the Nernst equation, **TPB-4N** demonstrated the unique oxidation behavior. However, the oxidation priority sequence in **TPB-4N** remains elusive and unclear, specifically, whether both electrons in the first two-electron transfer originate from the

 © 2025 Wiley-VCH GmbH

16136829, 0, Downloaded from https://onlinelibrary.wiley.com/doi/10.1002/smll.202508301 by National Taiwan University, Wiley Online Library on [12/11/2025]. See the Terms and Conditions (https://onlinelibrary.wiley.com/terms-and-conditions) on Wiley Online Library for rules of use; OA articles are governed by the applicable Creative Commons License

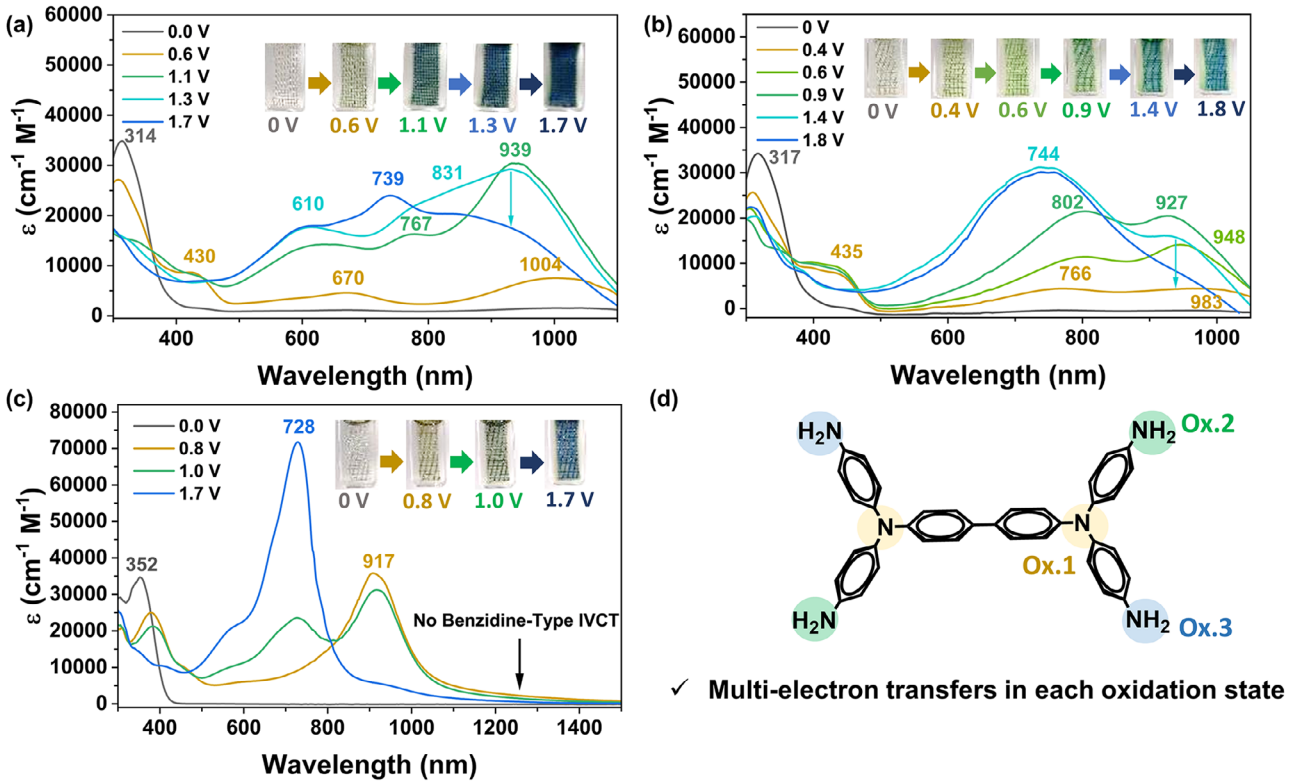

Figure 3. a–c) Spectroelectrochemistry diagram of a) **TPPA-2N**, b) **TPPA-4N**, and c) **TPB-4N**. All the samples were measured in an OTTLE cell with a platinum net electrode. (Sample amount: 0.5 μmol (5×10^{-4} M) in 1 mL of 0.1 M $TBABF_4$/GBL.) d) Supposed oxidation site priority in **TPB-4N**.

arylamine moiety or if one of the electrons is contributed by the primary amine. To clarify the oxidation sequence, theoretical simulations were conducted using density functional theory (DFT) with the B3LYP/6-31G(d,p) basis set under acetonitrile conditions. Natural bond orbital (NBO) analysis was employed to obtain the atomic charge distribution. The neutral, cation, and dication forms of **TPB-4N** were optimized, and Figure S6 (Supporting Information) shows that the charges of all electroactive nitrogens exhibited a symmetric distribution in the neutral form. In the cation form, the charges on the triarylamine centers (13N and 14N) were −0.402 and −0.331, respectively, while the four nitrogens on the *p*-phenylamino arms displayed varying values depending on their position on the phenyl arms (39N and 42N: −0.810; 40N and 41N: −0.848), indicating that the first electron transfer likely occurs at one of the arylamine nitrogens in the TPB moiety. In the dication form, the charge on 13N increased significantly to −0.318, and 14N also changed to the same charge value as 13N. The nitrogens on the four *p*-phenylamino arms also returned to identical charge values of −0.787. These findings suggest that the oxidation potential begins with 13N and is subsequently followed by 14N. Owing to it still undergoing a two-electron transfer at the second oxidation stage, we speculated that two of the *p*-phenylamino arms would be oxidized symmetrically. Thus, it is evident that the first two-electron transfer depicted in Figure 2a originates entirely from the arylamine nitrogens in **TPB-4N** rather than the nitrogens of the *p*-phenylamino arms, and the supposed oxidation sequence is illustrated in Figure 3d.

To simulate the practical usability, 15 000 (first oxidation state) and 10 000 (second oxidation state) continuous CV scans were conducted to evaluate the reversibility and cyclic stability of the resulting TAA derivatives. During the first 1000 cycles, all the TAAs revealed outstanding stability, and the shapes of the CV profiles remained steady (Figure S7, Supporting Information). Moreover, the UV-vis spectra also reveal the absorbance of each distinct peak of TAA in the neutral state without a noticeable decrement (**Figure** 4a–f; Figure S8, Supporting Information), and all maintained above 99% retention (Figure 4g), implying that no electrochemical side reaction or decomposition occurred. As the cycle number increased to 15 000 cycles, **TPPA-2N** still displayed the exact shape of the CV profile, with an optical retention of 97.0% among the TAAs monitored by UV–vis spectra, indicating high cyclic stability. On the contrary, the fully amino-substituted **TPPA-4N** and **TPB-4N** have excellent optical retention of up to 99.0% and 98.2%, and they also maintain the CV profile shapes, demonstrating the gratifying reversibility of all TAAs in the first oxidation state. In the second oxidation state, **TPB-4N** exhibits a straightforward distortion of CV profiles after 10 000 cycles, with optical retention of the distinct peak at ≈94.7%. A minor absorption is generated in the neutral state from 450 to 550 nm. **TPPA-2N** and **TPPA-4N** could preserve CV shape well and maintain optical retention at ≈95.0% and 95.2%, respectively. The outstanding reversibility of the oxidized TAAs is ascribed to the IV-CT resonance via the π-bridge to stabilize the formed cation radicals. Also, the generated dication radicals can resonate to form the benzoquinonediiminium moiety in the second oxidation state,

© 2025 Wiley-VCH GmbH

16136829, 0, Downloaded from https://onlinelibrary.wiley.com/doi/10.1002/smll.202508301 by National Taiwan University, Wiley Online Library on [12/11/2025]. See the Terms and Conditions (https://onlinelibrary.wiley.com/terms-and-conditions) on Wiley Online Library for rules of use; OA articles are governed by the applicable Creative Commons License

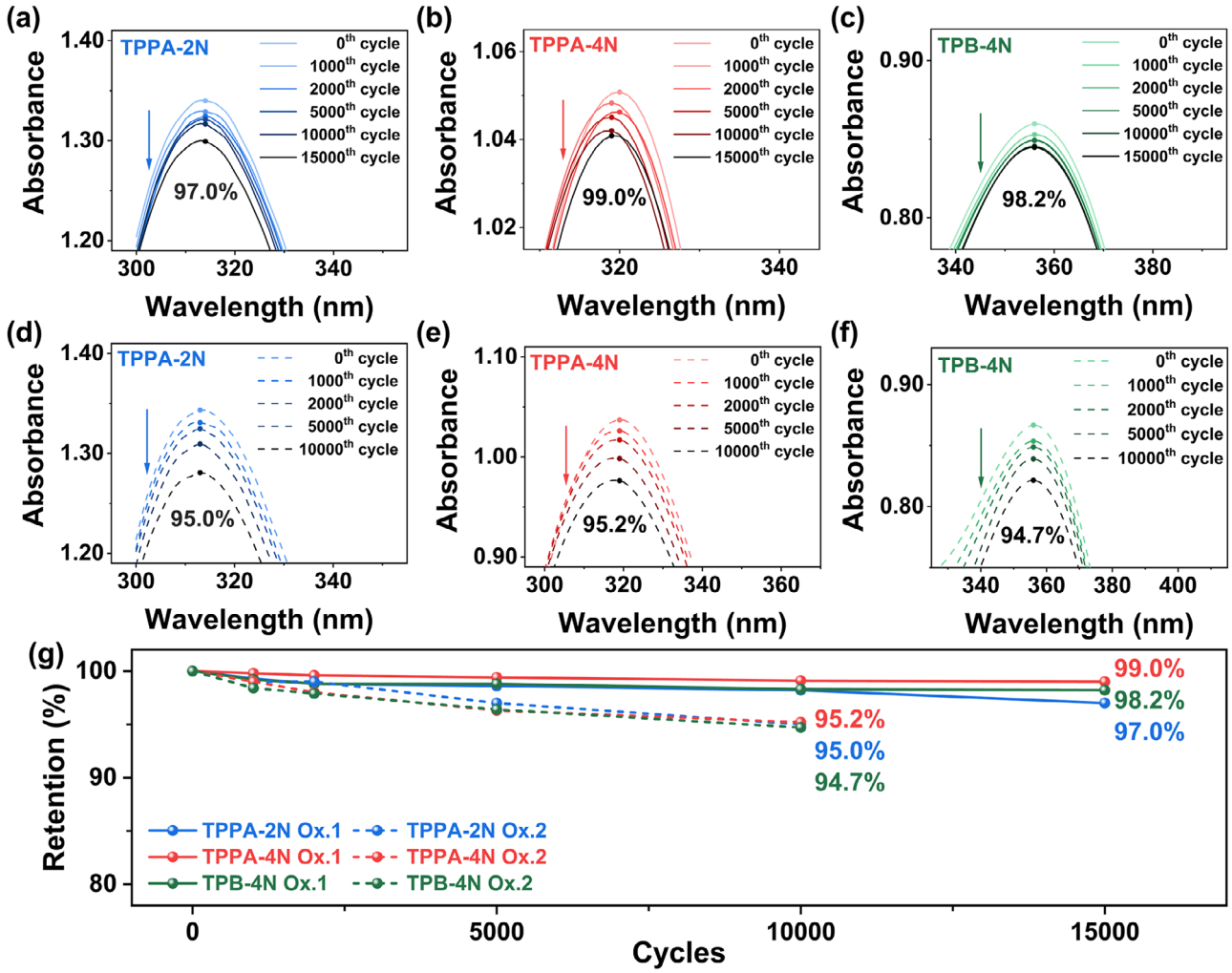

Figure 4. a–c) The first and d–f) second oxidation spectrochemical stability of **TPPA-2N, TPPA-4N,** and **TPB-4N** after different scanning cycles. The measurements were carried out in a 1 cm × 1 cm × 4 cm standard quartz cuvette with a 0.6 cm × 2.5 cm ITO-coated glass electrode. (Sample amount: 1.75 µmol (5×10^{-4} M) in 3.5 mL of 0.1 M $TBABF_4$/GBL). g) Plot of the reversibility retention comparison after different scanning cycles.

as depicted in Scheme S1 (Supporting Information). These results indicate that the TPPA architecture with multiple amino substituents could effectively enhance the reversibility and optical stability in the first and second oxidation states, demonstrating great potential for the practical use of the primary amino-containing triarylamine materials.

2.3. Electrochromic Properties of the Prepared ECDs

The liquid-type ECDs were further fabricated to elucidate the adaptability and applicability of the analyzed TAAs, as well as the specific methods outlined in the *Supporting Information*. In this context, heptyl viologen (HV) was utilized as the complementary cathodic material, which has already been proven to lower the applied voltage and increase the stability of ECDs (**Figure 5a**; Figure S9, Supporting Information).[33,48] The basic DPV and CV measurements of TAA devices are illustrated in Figures S10–S13 (Supporting Information). Similar to the tendency concluded from pristine TAAs, **TPPA-4N/HV** exhibited the lowest first and second oxidation potentials of 0.64 and 0.96 V, with the smallest ΔE and a symmetric CV profile, illustrating again the effectiveness of the amino groups and the phenyl π bridge. **TPPA-2N/HV** displayed the redox pairs at 0.76/0.55, 1.06/0.87, and 1.54/1.46 V, while **TPB-4N/HV** showed relatively higher potentials of 0.99/0.57, 1.23/1.04, and 1.63/1.39 V. The spectroelectrochemical measurements were applied at voltages not exceeding 2.0 V, ensuring the applied voltage was within the mitigatory range for the solvent-durable potential window. Figure S11 (Supporting Information) displays the appearance of **TPPA-2N/HV,** a colorless and transparent device (L*: 90.07, a*: –2.02, b*: 0.67) in the neutral state, and the absorbance of peaks at 437, 609, and 973 nm have gradually increased as the applied potential was raised to 0.8 V, changing the color to dark teal appearance (L*: 41.95, a*: –37.55, b*: –14.63). Note that the absorption at the center of 609 nm was attributed to the characteristic peak and resulting color of HV in the reduced state.[33,48] When applying voltage to the second and third oxidation states,

© 2025 Wiley-VCH GmbH

16136829, 0, Downloaded from https://onlinelibrary.wiley.com/doi/10.1002/smll.202508301 by National Taiwan University, Wiley Online Library on [12/11/2025]. See the Terms and Conditions (https://onlinelibrary.wiley.com/terms-and-conditions) on Wiley Online Library for rules of use; OA articles are governed by the applicable Creative Commons License

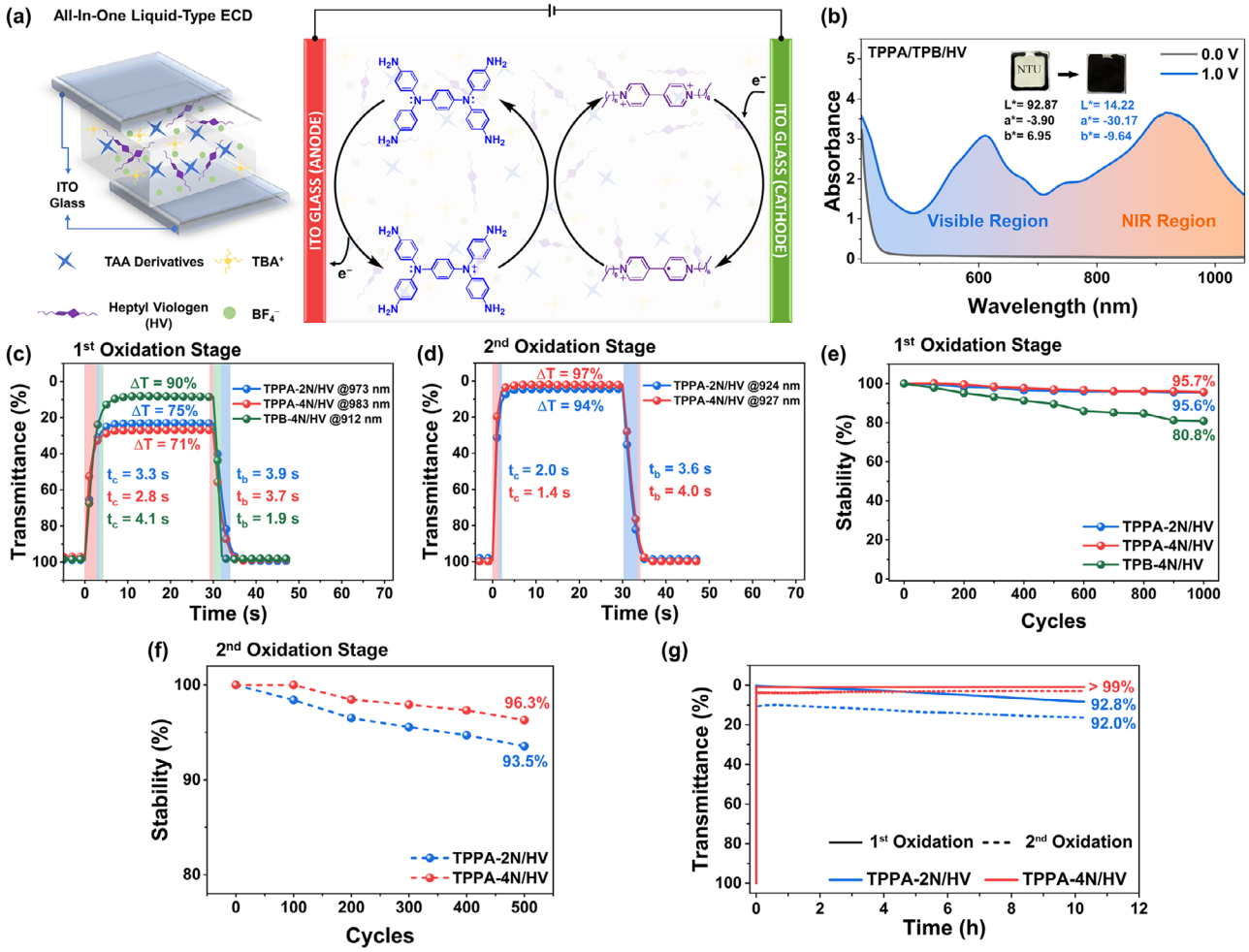

Figure 5. a) Configuration of the EC device and the mechanism after adding HV as a supplement cathodic EC material. b) Spectroelectrochemistry of blending ECD with a composition of 0.24 μmol **TPPA-4N** (0.005 M), 0.48 μmol **TPB-4N** (0.010 M), 1.44 μmol HV (0.060 M), and 4.8 μmol $TBABF_4$ (0.1 M) in 0.048 mL GBL. c) Switching response time of **TPPA-2N/HV**, **TPPA-4N/HV**, and **TPB-4N/HV** at first oxidation state. d) Switching response time of **TPPA-2N/HV** and **TPPA-4N/HV** at the second oxidation state. e,f) Switching stability of the TAA-based ECDs at the first and second oxidation stages. g) Long-term stability of TAA-based ECDs at the on-state for 10 h.

TPPA-2N/HV could change the appearance to Prussian blue (L*: 20.04, a*: –22.73, b*: –28.35) and then dark blue (L*: 6.86, a*: 0.64, b*: –29.04). **TPPA-4N/HV** also displayed a colorless and transparent appearance in the neutral state (L*: 89.38, a*: –2.96, b*: 3.07) and changed to green (L*: 46.18, a*: –44.88, b*: 0.09), dark green (L*: 25.17, a*: –39.57, b*: –18.72), and then dark blue (L*: 12.24, a*: –5.81, b*: –32.89), which is obviously different from **TPPA-2N/HV** (Figure S12, Supporting Information). It is worth noting that **TPPA-2N/HV** and **TPPA-4N/HV** manifested the polyelectrochormic features with three-stage color changes. Meanwhile, in **TPB-4N/HV** only exhibited two-stage color changes, changing from colorless (L*: 88.35, a*: –4.31, b*: 6.48) to dark slate gray (L*: 24.33, a*: –18.55, b*: –16.67) and the final dark blue (L*: 7.29, a*: –4.53, b*: –25.80) (Figure S13, Supporting Information). Nevertheless, it was found that the device derived by each of the TAA needs a high applied voltage (at least 1.7 V) to afford a darkening color. Hence, we posed the following question: What if we merged **TPPA-4N** and **TPB-4N** at a specific ratio? Would the resulting ECD perform a darkening color or even a black color under a lower applied potential? Therefore, Figure 4a and Figure S14 (Supporting Information) demonstrate the prepared ECD by mixing **TPPA-4N** and **TPB-4N** in a molar ratio of 1 to 2, maintaining the same total mole amount of the anodic materials as the abovementioned ECDs derived from only one TTA of 0.72 μmol. In the neutral state, the **TPPA/TPB/HV** still retained a colorless and transparent appearance (L*: 92.87, a*: –3.90, b*: 6.95) and could turn to a dense dark appearance when applying only 1.0 V, not only reducing nearly half of the applied voltage but also achieving the energy-saving efficacy. Although some wavelengths are not well absorbed (e.g., 500 nm) (Figure 5a), as the CIELAB value of L*: 14.22, a*: –30.17, b*: –9.64 (Figure 5b), **TPPA/TPB/HV** displayed a wide and broad absorption in the visible–NIR region with low applied driving voltage from other positive perspectives.

Moreover, except for the polyelectrochromic features, the response time (t_c and t_b for coloring and bleaching, respectively), coloration efficiency (ηCE), and long-term stability are crucial

© 2025 Wiley-VCH GmbH

16136829, 0, Downloaded from https://onlinelibrary.wiley.com/doi/10.1002/smll.202508301 by National Taiwan University, Wiley Online Library on [12/11/2025]. See the Terms and Conditions (https://onlinelibrary.wiley.com/terms-and-conditions) on Wiley Online Library for rules of use; OA articles are governed by the applicable Creative Commons License

and pivotal factors in realizing commercially practical products.[3] Among all the prepared ECDs, **TPPA-4N/HV** revealed the quickest response time either in the first (t_c/t_b: 2.8/3.7 s) or second (t_c/t_b: 1.4/4.1 s) oxidation state, as illustrated in Figure 5c,d. Meanwhile, **TPPA-2N/HV** (t_c/t_b: 3.3/3.9 s for the first oxidation; t_c/t_b: 2.0/3.6 s for the second oxidation) and **TPB-4N/HV** (t_c/t_b: 4.1/1.9 s) revealed lower response capability. These results are summarized and tabulated in **Table 2**. Furthermore, the coloration rate constants (k_c) according to the equation in the *Supporting Information* reveal that **TPPA-4N/HV** displayed the most gratifying values in the first (0.668 s^{-1}) and second (0.708 s^{-1}) coloring stages, while **TPPA-2N/HV** exhibited 0.396 and 0.351 s^{-1} for the first and second coloring stages, and **TPB-4N/HV** showed the lowest value of 0.314 s^{-1} (Figure S15, Supporting Information). These results suggest that **TPPA-4N** with four *para*-aminophenyl arms could facilitate enhanced electrochemical kinetics, leading to reduced coloration times in ECD. Likewise, η_{CE} also demonstrated the same trend that **TPPA-4N/HV** performed the higher values of 224 and 308 $cm^2\ C^{-1}$ for the first and second oxidation, respectively, while **TPPA-2N/HV** showed 197 and 302 $cm^2\ C^{-1}$ and 289 $cm^2\ C^{-1}$ for **TPB-4N/HV**, as summarized in (Figure S16, Supporting Information).

The switching stability test indicated that **TPPA-2N/HV** and **TPPA-4N/HV** could maintain excellent retention above 95% after 1000 switching cycles (cycle time: 60 seconds) in the first oxidation state, and the transmittance decay was only 3% (Figure 5e,f; Figure S17, Supporting Information). Conversely, **TPB-4N/HV** exhibited moderate retention of 80.8% after 1000 switching cycles with a transmittance decay of 16.4%. Furthermore, upon applying to the second oxidation state, **TPPA-2N/HV** retained a stability of 94% after 500 switching cycles, with a transmittance decay of 6%. In contrast, **TPPA-4N/HV** demonstrated superior stability of 96% after 500 switching cycles, with a transmittance decay of only 3.6%. Additionally, **TPPA-2N/HV** and **TPPA-4N/HV** underwent long-term ON-state measurement for 10 h to evaluate their long-term stability, as shown in Figure 5g. By this measurement, the differences in stability between these two devices became more pronounced: the stability of **TPPA-2N/HV** revealed 92.8% and 92.0% after a 10-h ON state in the first and second oxidation, respectively. In comparison, **TPPA-4N/HV** still performed with gratifyingly superior stability of 99% in both oxidation states. These results confirm that the presence of more amino functional groups and shorter π bridges can effectively enhance EC stability.

2.4. Photoluminescence (PL) and Electrofluorochromism (EFC) of TAAs

Except for the absorption properties, all TAAs revealed emissive properties in the solution state, and this behavior suggests that the TAAs have the potential to be applied in EFC applications. Hence, we investigated the PL behaviors of TAAs in various organic solvents, as shown in Figures S18 and S19 (Supporting Information), where **TPPA-2N** and **TPPA-4N** revealed no apparent trend of emission wavelength shifting or the quantum efficiency (Φ_{PL}) floating upon the different polarity of the solvent (Tables S5 and S6, Supporting Information). The emission wavelength (λ_{em}) for **TPPA-2N** and **TPPA-4N** in the GBL solution was 440 and 449 nm, respectively, and the Φ_{PL} was estimated to be 9.9% and 8.4%. In contrast, **TPB-4N** exhibited a significant solvent effect, such that the emission color could change from sky blue (461 nm) to green (531 nm) with a wavelength change of 70 nm owing to the central biphenyl bridge, which could be twisted at higher polarity solvents, and the Φ_{PL} values decreased dramatically from 24.6% to 1.3% (Table S7, Supporting Information). In addition, we investigated the aggregation-induced emission (AIE) behavior of the prepared TAAs by employing ethyl acetate (EA) as a good solvent and hexane as a poor solvent, in varying fractions. As shown in Figure S20 (Supporting Information), **TPPA-2N** exhibited no significant change in emission intensity with increasing proportion of poor solvent, whereas **TPPA-4N** and **TPB-4N** demonstrated pronounced aggregation-induced emission enhancement (AIEE). Consistent with our previous report and other literature, the use of a gel-type electrolyte can simulate the collective molecular environment by restricting intramolecular motions, thereby enhancing emission intensity in the corresponding EFCD.[32,56] Consequently, the EFCDs were fabricated using a gel-type electrolyte with an extra 10 wt.% of PMMA and a composition similar to the corresponding ECDs. After applying the driving potential, **TPPA-2N/HV** started to quench the emission intensity at 0.5 V and exhibited an ICR of 44 at 0.9 V (first oxidation state), as depicted in Figure S21 (Supporting Information). Surprisingly, **TPPA-4N/HV** started to quench at only 0.3 V, manifesting an ICR of 76 in the first oxidation potential (0.7 V), and could be further increased to 493, 859, and the extraordinary 950 when gradually increased stepwise by 0.1 V to the second oxidation state (1.0 V), as depicted in **Figure 6**a,c and Movie S1 (Supporting Information). On the other hand, **TPB-4N/HV** began quenching at 0.5 V and could exhibit a gratifyingly high ICR value of 393 at 1.0 V (Figure 6b).

Table 2. The electrochromic parameters of ECDs.

Index	1st oxidation state					2nd oxidation state				
	t_c [s] [a]	t_b [s] [b]	ΔT [%] [c]	η_{CE} [$cm^2\ C^{-1}$] [d]	k_c [s^{-1}] [e]	t_c [s] [a]	t_b [s] [b]	ΔT [%] [c]	η_{CE} [$cm^2\ C^{-1}$] [d]	k_c [s^{-1}] [e]
TPPA-2N	3.3	3.9	75	197	0.396	2.0	3.6	94	302	0.351
TPPA-4N	2.8	3.7	71	224	0.668	1.4	4.1	97	308	0.708
TPB-4N	4.2	1.9	90	289	0.314	–	–	–	–	–

[a] coloring time from the bleaching state to 90% of the total transmittance change; [b] bleaching time from the coloring state to 90% of complete transmittance change; [c] difference in transmittance is $\Delta T = T_b - T_c$, where T_b and T_c are the transmittances of bleaching and coloring states, respectively; [d] coloration efficiency is determined by the slope of change in optical density (ΔOD) versus charge density. Change in optical density is defined as $\Delta OD = \log [T_b/T_c]$; [e] the optical coloration rate constant (k_c) is calculated by the fitting lines of the plots of ΔOD versus time (s)

© 2025 Wiley-VCH GmbH

16136829, 0, Downloaded from https://onlinelibrary.wiley.com/doi/10.1002/smll.202508301 by National Taiwan University, Wiley Online Library on [12/11/2025]. See the Terms and Conditions (https://onlinelibrary.wiley.com/terms-and-conditions) on Wiley Online Library for rules of use; OA articles are governed by the applicable Creative Commons License

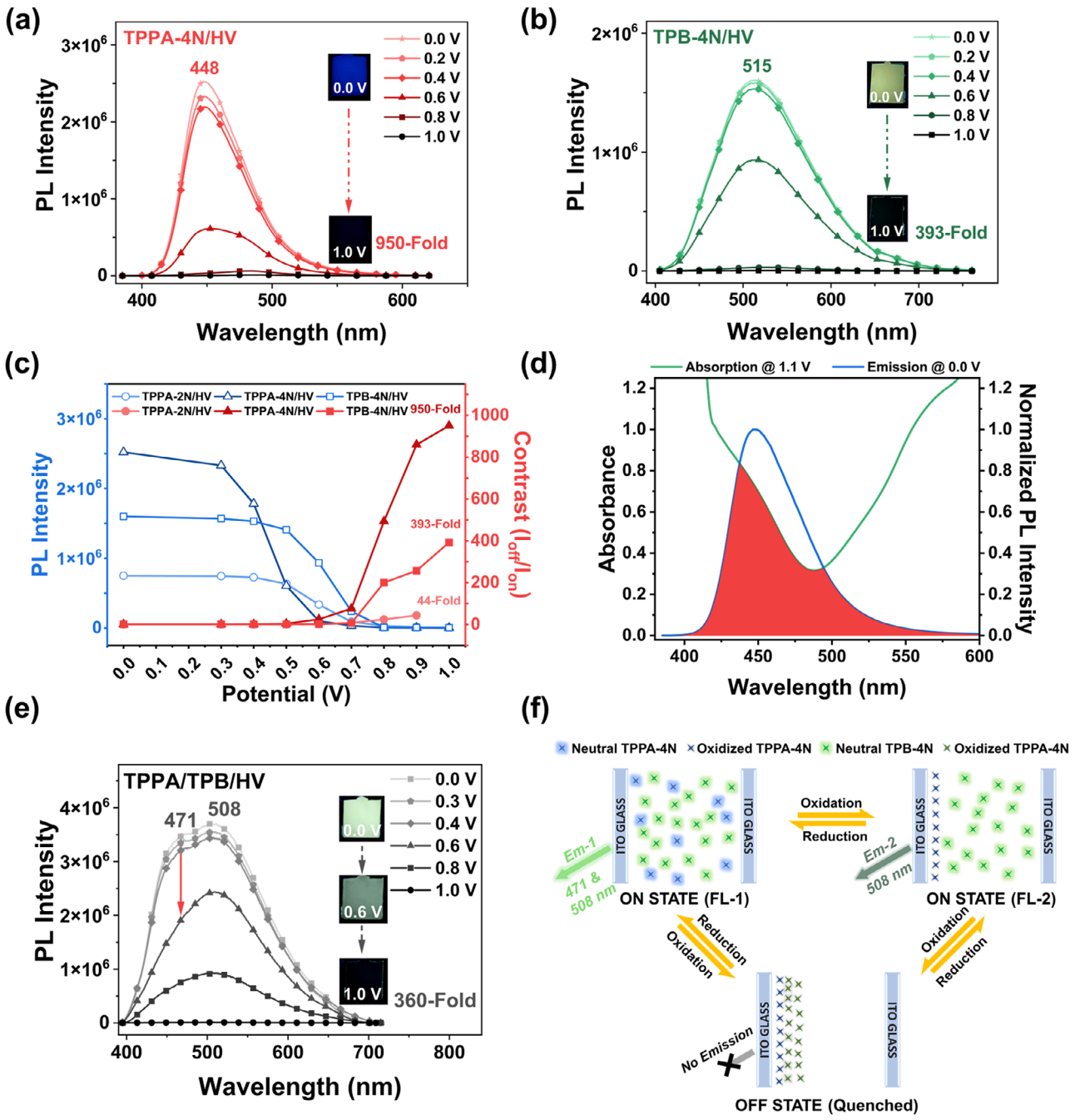

Figure 6. The EFC behaviors of a) **TPPA-4N/HV** and b) **TPB-4N/HV** EFCDs in the PL intensity versus various applied potentials. c) A double-Y axis plot using potential versus PL and intensity contrast ratio of TAA-based EFCDs. d) Absorption spectrum of **TPPA-4N/HV** ECD at 1.1 V versus the normalized PL spectrum of **TPPA-4N/HV** EFCD at 0.0 V to illustrate the self-absorption effect. e) **TPPA/TPB/HV** EFCD in the PL intensity versus various applied potentials. f) The schematic presentation of the mechanism for the authentic fluorochromism. The gel-type EFCDs were fabricated from ITO glasses with a 2 × 2 cm^2 active area. (sample amount: 0.72 μmol TAA derivatives (0.015 M), 1.44 μmol HV (0.060 M), and 4.8 μmol $TBABF_4$ (0.1 M) in 0.048 mL GBL (10 wt.% PMMA)).

Generally, small molecule-based EFCD is more challenging to reach an extremely high ICR value than polymer-based EFCD, owing to the difficulty of quenching for all the redox-active molecules in the device. To our knowledge, we have collected and summarized the ICR values from the references in Table S8 (Supporting Information), demonstrating that TPPA-4N/HV in this work is one of the few EFC materials that can reach an ICR value above 900. To address this issue, we compared the **TPPA-4N/HV** device absorption spectrum at 1.1 V (cf. Figure S12b, Supporting Information) with the PL spectrum at 0 V (cf. Figure 6a). The emission peak of **TPPA-4N** in EFCD was at 448 nm, and its characteristic absorption in the first and second oxidation

© 2025 Wiley-VCH GmbH

16136829, 0, Downloaded from https://onlinelibrary.wiley.com/doi/10.1002/smll.202508301 by National Taiwan University, Wiley Online Library on [12/11/2025]. See the Terms and Conditions (https://onlinelibrary.wiley.com/terms-and-conditions) on Wiley Online Library for rules of use; OA articles are governed by the applicable Creative Commons License

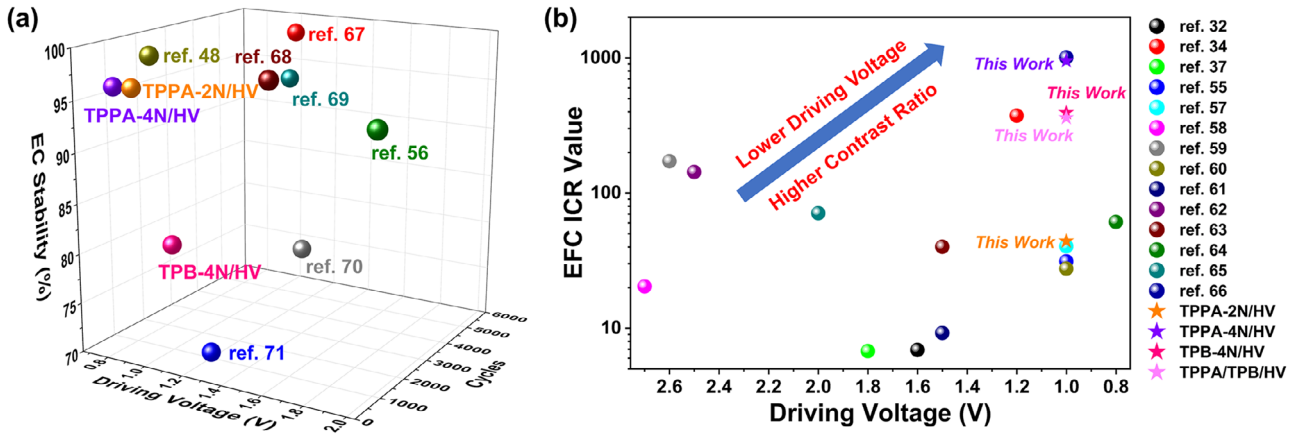

Figure 7. Plots of small molecule-based (a) ECD and (b) EFCD performance of the TAAs compared to the recent reference.

potentials was at 450 nm, implying that the oxidized **TPPA-4N** itself can absorb the emission from the remaining non-oxidized **TPPA-4N**, further to achieve a high ICR value, as illustrated in Figure 6d. Besides, **TPB-4N/HV** EFCD could also reveal an ICR value of 392-fold. Although **TPPA-2N/HV** EFCD also showed self-absorption tendency between the absorption and emission spectra, the PL intensity is much lower than that of **TPPA-4N/HV** EFCD, and the electrochemical kinetics are unsatisfactory, making it only perform an ICR value of 44. To illustrate the high ICR value of **TPPA-4N/HV** EFCD, we conducted the time-resolved photoluminescence spectroscopy measurement. As depicted in Figure S22 (Supporting Information), the lifetime of **TPB-4N/HV** EFCD decreases significantly from 0.72 ns in the FL-ON state to 0.16 ns in the FL-OFF state, and the lifetime profile in the FL-OFF state nearly overlaps with the IRF profile. Additionally, for **TPPA-4N/HV** EFCD, the lifetime can only be detected in the FL-ON state, with a value of 1.27 ns. In contrast, no observable lifetime is detected in the FL-OFF state due to the instrument limitations, indicating that the self-absorption effect in **TPPA-4N/HV** EFCD is the primary factor contributing to the high ICR value.

In addition, the response time (t_{ON}/t_{OFF}) of **TPPA-4N/HV** EFCD for emission quenching also demonstrated quick response capabilities of 3.6/11.1 s and 1.8/12.5 s in the first and second oxidation stages, respectively (Figure S23a,b, Supporting Information). Tables S8 and S9 (Supporting Information) tabulate and summarize the recent EFC studies on small-molecule and polymeric materials. The results demonstrate that EFCD derived from small-molecule materials of **TPPA-4N/HV** exhibits extraordinary capabilities in achieving high ICR and rapid response simultaneously. To illustrate the superior performance of the TAAs in this work, we have summarized comparative data for both small molecule-based EC and EFC devices, reported in recent years, as shown in **Figure 7**.[32,34,37,48,55,57–72] Notably, the TAA-based ECDs developed here require a lower driving potential to achieve high contrast ratios and exhibit excellent switching stability. Furthermore, the corresponding EFCD devices display higher ICR values at lower driving potentials compared to most literature examples, as illustrated in Figure 7b. These results highlight the potential of TAAs as promising candidates for practical applications.

Furthermore, we attempted another more intriguing approach, the composed blending ECFD of **TPPA/TPB/HV**, to demonstrate spectacularly authentic "potential-modulated fluorochromism" behavior, as presented in Figure 6e,f and Movie S2 (Supporting Information), which exhibited the two-stage emission color change from the merging lime green emission color (471 and 508 nm at 0.0 V) to olive green emission color (508 nm at 0.6 V) and then quenched reversibly (at 1.0 V) with a 360 ICR value. In Figure 6a,b, it is evident that **TPPA-4N/HV** EFCD requires a lower driving potential to induce emission quenching, with the emission dramatically quenched at 0.6 V. At the same time, **TPB-4N/HV** EFCD only begins to quench. This result demonstrates that **TPPA/TPB/HV** EFCD possesses a sufficiently wide potential window for operation. Besides, the emission wavelength of **TPB-4N/HV** EFCD is at 515 nm, which does not overlap with the main absorption band of oxidized **TPPA-4N** (Figure 6d). As a result, the emission from neutral **TPB-4N** remains clearly observable, enabling a unique two-stage emission color change. To our knowledge, although A. Beneduci et al. reported a series of triarylamine small molecules exhibiting electrochemically fluorescent chromism by calculating the CIE coordinates (CIE 1931), achieving corresponding small molecule-based EFCD with these unique fluorochromes via an electrochemical process remains challenging.[73] Most of the reported EFCDs mainly displayed the emissive to quenched states with only one emission color. Our new finding enables an up-and-coming EFC family to achieve and realize real multi-stage "fluorochromism" via a facile and judicious blending approach.

3. Conclusion

This study develops and evaluates various *para*-amino-substituted TAAs (**TPPA-2N**, **TPPA-4N**, and **TPB-4N**) to tailor EC and EFC characteristics. Among them, the **TPPA-4N/HV** device exhibited outstanding performance, with exceptionally high stability (96% retention after 1000 switching cycles and 99% retention after a 10-h switching ON state) both in the first and second oxidation states, low driving potential (0.7 V), high coloration efficiency (308 cm^2 C^{-1}), quick response capability, and an extraordinary and impressive electrofluorochromic ICR value of 950. Consequently, the *para*-aminophenyl arms

© 2025 Wiley-VCH GmbH

16136829, 0, Downloaded from https://onlinelibrary.wiley.com/doi/10.1002/smll.202508301 by National Taiwan University, Wiley Online Library on [12/11/2025]. See the Terms and Conditions (https://onlinelibrary.wiley.com/terms-and-conditions) on Wiley Online Library for rules of use; OA articles are governed by the applicable Creative Commons License

could increase the electron-donating capability, reduce oxidation potentials, and promote fluorescence quenching efficiency. Furthermore, by merging two TAA molecules (**TPPA-4N** and **TPB-4N**), the resulting EFCD exhibits reversible two-stage EFC behavior, transitioning from lime to olive green emission and then completely quenching during the switching-on oxidation procedure. Additionally, we observed that the phenyl π-bridge in TPPA derivatives further enhances resonance effects compared to the biphenyl π-bridge in the TPB counterpart, resulting in exceptionally superior electrochemical stability and electrochemical performance. These findings demonstrate that the scalable yet straightforward synthesis strategy of **TPPA-4N** reveals impressive potential as an up-and-coming high-performance material for advanced EC and EFC applications.

4. Method Section

4.1. Calculations

4.1.1. Optical Coloration Rate Constant Calculation

The coloration rate constant (k_c) can be calculated by the infinitesimal difference of absorbance (dA) at a specific wavelength at any time (t) and is given by:

$$dA\,(t) = l\varepsilon_{ox} dc_{ox}\,(t) \tag{2}$$

where l is the sample optical length, ε_{ox} is the molar extinction coefficient, and $dc_{ox}(t)$ is the infinitesimal difference in the concentration of the radical cation species. By integrating Equation (1), we can obtain the difference in the optical density of the sample at any t:

$$\Delta OD = l\varepsilon_{ox}\left[c_{ox}\,(t) - c_{ox}\,(0)\right] = l\varepsilon_{ox} c_{ox}\,(t) \tag{3}$$

where $c_{ox}(0)$ equals to 0. To estimate the concentration of the radical cation at any t in the device, we assume that the heterogeneous electron transfer reactions at the ITO electrode are of first order with rate coefficients k. The rate of difference of $c_{ox}(t)$ could therefore be expressed as:

$$\frac{d}{dt} c_{ox}\,(t) = k_c c_{neutral}\,(t) = k_c\left[c_{neutral}\,(0) - c_{ox}\,(t)\right] \tag{4}$$

where $c_{neutral}(t)$ is the concentration of the precursor species at any t and k_c is the coloration rate constant. After integrating Equation (3), the obtained equation can express the concentration of the radical cation species as a function of t:

$$c_{ox}\,(t) = c_{neutral}\,(0) - A_1 e^{-k_c t} \tag{5}$$

$$\Delta OD = l\varepsilon_{ox} c_{neutral}\,(0) - A_1 l\varepsilon_{ox} e^{-k_c t} \tag{6}$$

Therefore, it will be an exponential function by plotting ΔOD versus t, thus getting the coloration rate constant (k_c).

4.1.2. Randles-Sevick Equation

$$i_p = 0.4463nFAC\left(\frac{nF\nu D}{RT}\right)^{\frac{1}{2}} \tag{7}$$

where i_p is the peak current (A), A is the electrode area (cm^2), and C is the concentration of **TAA**s (mol cm^{-3}).

Supporting Information

Supporting Information is available from the Wiley Online Library or from the author.

Acknowledgements

Y.-J.S. and P.-Y.L. contributed equally to this work. The authors gratefully thank Prof. Pi-Tai Chou from the Department of Chemistry, National Taiwan University, for his assistance with the time-resolved fluorescence measurement. This work is funded by the National Science and Technology Council in Taiwan (NSTC 113-2221-E-002-061-MY3 and 111-2221-E-002 -028 -MY3).

Conflict of Interest

The authors declare no conflict of interest.

Data Availability Statement

Research data are not shared.

Keywords

electrochromic, electrofluorochromic, multi-amino substitution, polyelectrochromic, triarylamine

Received: July 9, 2025
Revised: November 4, 2025
Published online:

[1] R. J. Mortimer, *Annu. Rev. Mater. Res.* **2011**, *41*, 241.
[2] J. Niu, Y. Wang, X. Zou, Y. Tan, C. Jia, X. Weng, L. Deng, *Appl. Mater. Today* **2021**, *24*, 101073.
[3] C. Gu, A.-B. Jia, Y.-M. Zhang, S. X.-A. Zhang, *Chem. Rev.* **2022**, *122*, 14679.
[4] Y. Zhai, J. Li, S. Shen, Z. Zhu, S. Mao, X. Xiao, C. Zhu, J. Tang, X. Lu, J. Chen, *Adv. Funct. Mater.* **2022**, *32*, 2109848.
[5] S. Kandpal, T. Ghosh, C. Rani, A. Chaudhary, J. Park, P. S. Lee, R. Kumar, *ACS Energy Lett.* **2023**, *8*, 1870.
[6] Y. Zhao, X. Zhang, W. Li, Z. Li, H. Zhang, M. Chen, W. Sun, Y. Xiao, J. Zhao, Y. Li, *Sol. Energy Mater. Sol. Cells* **2022**, *237*, 111564.
[7] J. Guo, H. Jia, Z. Shao, P. Jin, X. Cao, *Acc. Mater. Res.* **2023**, *4*, 438.
[8] S. K. Deb, *Sol. Energy Mater. Sol. Cells* **2008**, *92*, 245.
[9] R.-T. Wen, C. G. Granqvist, G. A. Niklasson, *Nat. Mater.* **2015**, *14*, 996.
[10] R. Li, X. Ma, J. Li, J. Cao, H. Gao, T. Li, X. Zhang, L. Wang, Q. Zhang, G. Wang, *Nat. Commun.* **2021**, *12*, 1587.
[11] K. R. Reyes-Gil, Z. D. Stephens, V. Stavila, D. B. Robinson, *ACS Appl. Mater. Interfaces* **2015**, *7*, 2202.
[12] M. Barawi, L. De Trizio, R. Giannuzzi, G. Veramonti, L. Manna, M. Manca, *ACS Nano* **2017**, *11*, 3576.
[13] P. M. Beaujuge, J. R. Reynolds, *Chem. Rev.* **2010**, *110*, 268.
[14] A. W. Lang, A. M. Österholm, J. R. Reynolds, *Adv. Funct. Mater.* **2019**, *29*, 1903487.

© 2025 Wiley-VCH GmbH

16136829, 0, Downloaded from https://onlinelibrary.wiley.com/doi/10.1002/smll.202508301 by National Taiwan University, Wiley Online Library on [12/11/2025]. See the Terms and Conditions (https://onlinelibrary.wiley.com/terms-and-conditions) on Wiley Online Library for rules of use; OA articles are governed by the applicable Creative Commons License

[15] I. Schwendeman, R. Hickman, G. Sönmez, P. Schottland, K. Zong, D. M. Welsh, J. R. Reynolds, *Chem. Mater.* **2002**, *14*, 3118.
[16] Y. Huang, B. Wang, F. Chen, Y. Han, W. Zhang, X. Wu, R. Li, Q. Jiang, X. Jia, R. Zhang, *Adv. Opt. Mater.* **2022**, *10*, 2101783.
[17] F. Zhao, B. Wang, W. Zhang, S. Cao, L. Liu, A. Y. Elezzabi, H. Li, W. Y. William, *Mater. Today* **2023**, *66*, 431.
[18] J.-L. Wang, S.-Z. Sheng, Z. He, R. Wang, Z. Pan, H.-Y. Zhao, J.-W. Liu, S.-H. Yu, *Nano Lett.* **2021**, *21*, 9976.
[19] H.-J. Yen, G.-S. Liou, *Prog. Polym. Sci.* **2019**, *89*, 250.
[20] D. T. Christiansen, A. e. L. Tomlinson, J. R. Reynolds, *J. Am. Chem. Soc.* **2019**, *141*, 3859.
[21] A. M. Österholm, L. Nhon, D. E. Shen, A. M. Dejneka, A. L. Tomlinson, J. R. Reynolds, *Mater. Horiz.* **2022**, *9*, 252.
[22] G. S. Collier, R. Wilkins, A. L. Tomlinson, J. R. Reynolds, *Macromolecules* **2021**, *54*, 1677.
[23] G. A. Corrente, A. Beneduci, *Adv. Opt. Mater.* **2020**, *8*, 2000887.
[24] H. Al-Kutubi, H. R. Zafarani, L. Rassaei, K. Mathwig, *Eur. Polym. J.* **2016**, *83*, 478.
[25] P. Audebert, F. Miomandre, *Chem. Sci.* **2013**, *4*, 575.
[26] S. Seo, Y. Kim, Q. Zhou, G. Clavier, P. Audebert, E. Kim, *Adv. Funct. Mater.* **2012**, *22*, 3556.
[27] R. Martínez, I. Ratera, A. Tárraga, P. Molina, J. Veciana, *Chem. Commun.* **2006**, 3809.
[28] R. Zhang, Z. Wang, Y. Wu, H. Fu, J. Yao, *Org. Lett.* **2008**, *10*, 3065.
[29] M. Chang, W. Chen, H. Xue, D. Liang, X. Lu, G. Zhou, *J. Mater. Chem. C* **2020**, *8*, 16129.
[30] N. Yan, W. Zhang, G. Li, S. Zhang, X. Yang, K. Zhou, D. Pei, Z. Zhao, G. He, *Mater. Chem. Front.* **2021**, *5*, 4128.
[31] R.-Z. Li, Q. Hao, X.-R. Ren, C. Wen, L. Wang, Z.-L. Zhao, J.-Y. Shao, Y.-W. Zhong, D. Wang, L.-J. Wan, *ACS Appl. Mater. Interfaces* **2024**, *16*, 49594.
[32] H.-T. Lin, C.-L. Huang, G.-S. Liou, *ACS Appl. Mater. Interfaces* **2019**, *11*, 11684.
[33] J. H. Wu, G. S. Liou, *Adv. Funct. Mater.* **2014**, *24*, 6422.
[34] H.-T. Lin, J.-T. Wu, M.-H. Chen, G.-S. Liou, *J. Mater. Chem. C* **2020**, *8*, 12656.
[35] T. Yu, P. Theato, H. Yao, H. Liu, Y. Di, Z. Sun, S. Guan, *Chem. Eng. J.* **2023**, *451*, 138441.
[36] N. Elgrishi, K. J. Rountree, B. D. McCarthy, E. S. Rountree, T. T. Eisenhart, J. L. Dempsey, *J. Chem. Educ.* **2018**, *95*, 197.
[37] S.-Y. Chen, Y.-W. Chiu, G.-S. Liou, *Nanoscale* **2019**, *11*, 8597.
[38] G. Kumar Silori, S. C. Chien, L. C. Lin, K. C. Ho, *Angew. Chem.* **2024**, *64*, 202416046.
[39] S. Xiong, M. Chen, J. Wu, F. Lv, K. Fang, K. Zhang, J. Guo, X. Cui, Y. Zhang, C. Hua, *Electrochim. Acta* **2024**, *497*, 144486.
[40] H. Chu, Y. You, J. Liang, Y. Hou, H. Niu, *ACS Appl. Polym. Mater* **2024**, *6*, 6800.
[41] Y. Gautier, W. Skene, *J. Mater. Chem. C* **2024**, *12*, 3589.
[42] D. Li, Y. Xu, J. Dai, Q. Qin, H. Fu, X. Wang, Y. Xu, B. Zeng, W. Luo, L. Dai, *J. Colloid Interface Sci.* **2025**, *684*, 11.
[43] Y.-J. Shao, T.-C. Yen, C.-C. Hu, G.-S. Liou, *J. Mater. Chem. A* **2023**, *11*, 1877.
[44] Y.-J. Shao, Y.-J. Cho, H.-L. Li, C.-C. Hu, G.-S. Liou, *J. Mater. Chem. A* **2024**, *12*, 20327.
[45] L. Huang, R. Guo, Q. Qiu, H. Li, P. Balla, J. Zeng, T. Liang, X. Qi, P. Liu, *Chem. Eng. J.* **2024**, *497*, 155018.
[46] D. Li, Y. Xu, J. Dai, H. Fu, X. Wang, Y. Xu, Q. Qin, A. Cabot, L. Dai, *Energy Storage Mater.* **2025**, *75*, 104036.
[47] A.-E. Bejan, C.-P. Constantin, M.-D. Damaceanu, *Mater. Today Chem.* **2022**, *26*, 101100.
[48] Y.-J. Shao, M.-H. Tu, G.-S. Liou, *Chem. Eng. J.* **2023**, *466*, 143003.
[49] H.-J. Yen, G.-S. Liou, *Chem. Mater.* **2009**, *21*, 4062.
[50] A. F. El-Mahdy, M. G. Mohamed, T. H. Mansoure, H.-H. Yu, T. Chen, S.-W. Kuo, *Chem. Commun.* **2019**, *55*, 14890.
[51] J. A. Davies, A. Tarzia, T. K. Ronson, F. Auras, K. E. Jelfs, J. R. Nitschke, *Angew. Chem., Int. Ed.* **2023**, *62*, 202217987.
[52] C. Lambert, G. Nöll, *J. Am. Chem. Soc.* **1999**, *121*, 8434.
[53] H.-J. Yen, K.-Y. Lin, G.-S. Liou, *J. Mater. Chem.* **2011**, *21*, 6230.
[54] A. V. Szeghalmi, M. Erdmann, V. Engel, M. Schmitt, S. Amthor, V. Kriegisch, G. Nöll, R. Stahl, C. Lambert, D. Leusser, *J. Am. Chem. Soc.* **2004**, *126*, 7834.
[55] J.-T. Wu, H.-T. Lin, G.-S. Liou, *ACS Appl. Mater. Interfaces* **2019**, *11*, 14902.
[56] J. Chen, C. C. Law, J. W. Lam, Y. Dong, S. M. Lo, I. D. Williams, D. Zhu, B. Z. Tang, *Chem. Mater.* **2003**, *15*, 1535.
[57] B. Gélinas, D. Das, D. Rochefort, *ACS Appl. Mater. Interfaces* **2017**, *9*, 28726.
[58] R. Huang, P. Li, Y. Xie, M. Zhou, F.-Q. Bai, Z. Chen, D. Chao, *Sol. Energy Mater. Sol. Cells* **2025**, *282*, 113400.
[59] S. Tripathi, S. Halder, P. Sivasakthi, P. K. Samanta, C. Chakraborty, M. Chakravarty, *Next Mater.* **2025**, *6*, 100472.
[60] Q. Tian, J. Xu, Y. Sha, X. Zhu, W. Chu, *Colloids Surf. A* **2024**, *694*, 134095.
[61] Y. Zhang, X. Jia, B. Sun, R. Huang, C. Wang, D. Chao, *Small* **2023**, *19*, 2301886.
[62] G. A. Corrente, D. A. González, E. Aktas, A. L. Capodilupo, F. Ruighi, G. Accorsi, D. Imbardelli, C. Rodriguez-Seco, E. Martinez-Ferrero, E. Palomares, A. Beneduci, *J. Mater. Chem. C* **2023**, *11*, 17115.
[63] T. J. Adams, A. R. Brotherton, J. A. Molai, N. Parmar, J. R. Palmer, K. A. Sandor, M. G. Walter, *Adv. Funct. Mater.* **2021**, *31*, 2103408.
[64] G. A. Corrente, E. Fabiano, M. La Deda, F. Manni, G. Gigli, G. Chidichimo, A.-L. Capodilupo, A. Beneduci, *ACS Appl. Mater. Interfaces* **2019**, *11*, 12202.
[65] D. Yu, E. Jang, Y. Wi, J. Hyeong, K. M. Lee, N. P. Godman, M. E. McConney, L. De Sio, S. I. Lim, K. U. Jeong, *Adv. Funct. Mater.* **2025**, *35*, 2420062.
[66] P. V. Navya, K. Ganesan, E. C. Neyts, S. Sampath, *Chem.–A Eur. J.* **2024**, *30*, 202401647.
[67] R. Huang, N. Cao, G. Gu, X. Jia, D. Chao, *Adv. Funct. Mater.* **2025**, 11224.
[68] F. Sun, H. Zhang, J. Cai, F. Su, Y. Tian, Y. J. Liu, *Sol. Energy Mater. Sol. Cells* **2023**, *250*, 112106.
[69] Q. Zhang, X. Liu, Y. He, M. Yan, I. Murtaza, D. Zou, T. Xu, Y. Cui, L. Zeng, H. Meng, *Chem. Eng. J.* **2025**, *516*, 164117.
[70] P. Gao, Y. Pan, H. Han, Z. Gu, H. Chen, Z. Wu, H. Liu, S. Peng, X.-P. Zhang, R. Zhang, *J. Mol. Struct.* **2023**, *1288*, 135769.
[71] B. Tao, M. Ouyang, Q. Hua, C. Kong, J. Zhang, W. Li, R. Bai, J. Liu, X. Lv, C. Zhang, *ACS Appl. Mater. Interfaces* **2023**, *15*, 13730.
[72] C. Qian, P. Wang, X. Guo, C. Jiang, P. Liu, *Sol. Energy Mater. Sol. Cells* **2024**, *266*, 112669.
[73] G. A. Corrente, D. A. González, E. Aktas, A. L. Capodilupo, G. Mazzone, F. Ruighi, G. Accorsi, D. Imbardelli, C. Rodriguez-Seco, E. Martinez-Ferrero, *Adv. Opt. Mater.* **2023**, *11*, 2201506.

© 2025 Wiley-VCH GmbH

16136829, 0, Downloaded from https://onlinelibrary.wiley.com/doi/10.1002/smll.202508301 by National Taiwan University, Wiley Online Library on [12/11/2025]. See the Terms and Conditions (https://onlinelibrary.wiley.com/terms-and-conditions) on Wiley Online Library for rules of use; OA articles are governed by the applicable Creative Commons License